Room-temperature ferromagnetism in oxidized-graphenic nanoplatelets induced by topographic defects

J.J. Prías-Barragán [a],[*], K. Gross [b], H. Ariza-Calderón [a], P. Prieto [b], C. Di Giorgio [c], F. Bobba [c],[d], A. M. Cucolo [c],[d]

[a] *Interdisciplinary Institute of Sciences, Doctoral Program in Physical Sciences, Electronic Instrumentation Technology Program at Universidad del Quindío, 630004 Armenia, Colombia*
[b] *Center of Excellence on Novel Materials (CENM), Department of Physics at Universidad del Valle, 25157 Cali, Colombia*
[c] *Physics Department "E.R. Caianiello", University of Salerno, Via Giovanni Paolo II 132, 84084 Fisciano, Italy*
[d] *CNR-SPIN, Via Giovanni Paolo II 132, 84084 Fisciano, Italy*

ARTICLE INFO

ABSTRACT

This work reports on room-temperature ferromagnetism of pyrolytic oxidized-graphene nanoplatelets obtained from bamboo pyroligneous acid by varying the density of extended defects. Topographic defects, created during the fabrication process, arise from a natural formation of clusters; such clusters drastically distort the graphitic basal plane, giving rise to abrupt surface curvatures. Topographic defects were found to be sources of the magnetic signal, as evidenced by bulk magnetization and magnetic force microscopy measurements. Increased defect density, tuned by carbonization temperature, results in enhanced magnetization.

1. Introduction

Recently, magnetism in graphene, reduced graphene oxide (rGO), and related materials is arising a growing interest due to its unconventional origin and possible technological applications [1–39]. Magnetism in graphene has been found to originate from [1] defects of different nature and length-scale point defects (vacancies, ad-atoms, etc.) [1–3]; extended defects (voids, cracks, etc.) [1,4]; crystal lattice defects (heptagons, pentagons, etc.) [1,5]; topological defects (corrugations, wrinkles, curvatures, etc.) [1]; and boundary defects (edges, grain boundaries, etc.) [1,6], among others.

Within this framework, considerable effort is made to provide a theoretical explanation of such defect-induced magnetism. For instance, first-principle calculations have been exploited to study the magnetic contributions of ad-atoms [1,6], hydrogen adsorption [7,8], vacancies (including single vacancy, H, Si, or N partially saturated vacancy, and vacancy clusters) [6,9–11] under coordinated atoms or edges [12], topological defects [3], surface curvature [1], as well as intrinsic magnetism in graphene systems [13]. By using first-principles calculations, Dutta et al., [14] report on the emergence of magnetic moments (in a range of 0.2–2.7 μB) in pristine graphene due to localized states at the grain boundaries as defects separating domains with different

crystallographic directions [14]. Then, the presence of defects in graphene play a special role in the ferromagnetic behaviour, because of carbon atoms into boundary defects can be out-plane, producing the stretching of the electron orbits, modifying the magnetic moment and spin–spin interaction of localized manner; then, when the external magnetic field is applied, the initial unordered state combined with the spin–spin interaction can produce alignment of magnetic moments with the external magnetic field applied; therefore, by increasing defect density, it is possible to increase the ferromagnetic order in graphene. Also, the appearance of magnetism has been further studied in curved graphene sheets. In particular, topological defects leading to graphene curvature, such as Stone-Wales defects caused by the rotation of carbon atoms can lead to localized spin moments [1]. Sharma *et al.*, [15] proposed that a ferromagnetic ground state can be expected in large deformed graphene. Evidence of ferromagnetic order at room temperature in metal-free, carbon-based structures has been reported through several experiments [9,16–25]. Studies of irradiated carbon structures have provided convincing proof of the defect-induced magnetic order. Irradiation with light ions (H+, He) can induce the formation of defects, such as vacancies, interstitial carbon atoms, vacancy-interstitial pairs (Frenkel pairs), and clusters. In these cases, unbounded electrons can strongly modify the crystal structure, providing a non-zero magnetic

* Corresponding author.
  E-mail address: jjprias@uniquindio.edu.co (J.J. Prías-Barragán).

moment. A review of irradiation-induced defects and their correlation with magnetic properties in graphitic systems can be found in Refs. [21,22].

In addition, oxygen-containing [carbonyl (C═O), carboxyl (─COOH), epoxy (C─O─C) etc.,], and/or hydroxyl (─OH) groups have been suggested as responsible for the induced magnetic moments in GO and rGO; however, experimental evidence seems to demonstrate that magnetism in these systems originates because of defect/vacancy states [9,10]. Table 1 lists the expected theoretical magnetic moments as calculated for several possible mechanisms responsible for ferromagnetism (FM) order in GO samples. One can observe that the highest contribution to ferromagnetism in GO is theoretically expected because of grain boundary defects with a magnetic moment of 2.76 μB/Å and hydrogen/OH chemisorption defects with magnetic moment around 1.00 μB/Å [14].

According to [14], extended defects in GO and rGO systems could, thus, play an important role in induced magnetization; nevertheless, to the best of our knowledge, no experimental evidence of this effect had been reported for these systems, as recently reported [26–29]. In previous reports by our group [30–37], we demonstrated that oxidized-graphene nanoplatelets obtained from bamboo pyroligneous acid (OGNP-BPA) show semiconductor-like behaviour with tuneable bandgap in a range of 0.11–0.30 eV. Herein, we focus on its room-temperature ferromagnetism as induced by topographic defects. Indeed, defects are created during the fabrication process, arising from a natural formation of clusters that drastically distort the graphitic basal plane, giving rise to step edges and abrupt surface curvatures. By employing atomic force microscopy and magnetic force microscopy (AFM/MFM) measurements, such defects are found as the source of non-zero magnetization, as measured by bulk techniques. Moreover, we have found enhanced magnetization by increasing defect density, tuned by the carbonization temperature. These results provide new experimental evidence of defect-induced magnetism in graphene-related materials without requiring high-cost ion bombardment experiments [19]. Moreover, the semiconducting nature of OGNP-BPA, combined with room-temperature (RT)-ferromagnetism raise hopes for low-cost, carbon-based novel information technologies. Therefore, this work presents room-temperature ferromagnetism in oxidized-graphenic nanoplatelets induced by topographic defects, as a systematic and fine way for describing magnetism in graphene-based materials.

2. Experimental section

2.1. Sample preparations

The OGNP samples were obtained by double-thermal decomposition (DTD) method in a pyrolysis system under controlled nitrogen atmosphere by using bamboo - *Guadua angustifolia* Kunth as source material. In a first pyrolysis step or thermal decomposition, the pyroligneous acid was obtained at 973 K and collected in a decanting funnel glass. In a second pyrolysis step, we used the pyroligneous acid as a source to obtain OGNP-BPA at different carbonization temperatures (TCA = 673, 773, 873, and 973 K). Powders of OGNP-BPA platelets were obtained by mechanical grinding and subsequent sonication, filtering, and selection

Table 1
Magnetic moments of each theoretical mechanism that seeks to explain FM order in graphene.

FM Mechanism	Magnetic Moment (μB/A)	References
Vacancy (Dangling bonds)	0.60–1.00	[6,7]
Hydrogen chemisorption	1.00–1.25	[7,8]
OH groups chemisorption	1.00	[24]
Zig-zag edge	0.01–0.35	[6]
Disordered graphene (Hubbard model)	0.01–0.15	[6]
Topological line defect	0.030–0.140	[13]
Grain boundary defects	1.732–2.707	[14]

procedures by using the Langmuir-Blodgett method. For more details on the synthesis method, please refer to [30,31].

2.2. Characterization methods

The OGNP-BPA were morphologically and chemically characterized by scanning electron microscopy (SEM) and energy-dispersive X-ray spectroscopy (EDS) by using a Phenom G2 Pro Microscopy field-emitting scanning electron microscope. Transmission electron microscopy (TEM) and high-resolution (HR)-TEM images were obtained by using the Tecnai F20 Super Twin TMP on a FEI microscope operating at 80 kV and equipped with a Cs image corrector and a Gatan Tridiem spectrometer. Correlations between the topography and magnetic signal were observed locally with AFM and MFM, using a NanoWizard III from jpk and employing the standard two-step technique. Bulk magnetization measurements were performed as a function of the external magnetic field, H, by using a PPMS Quantum-Design system. Correlations between defect density and carbonization temperature were obtained by employing Raman spectroscopy. Raman spectra were recorded with a confocal Raman Horiba Jobin Yvon, model Labram HR at room temperature, with a 632.8 nm wavelength, and 0.25 mW of HeNe laser power.

3. Results and discussion

3.1. Topographic defects on individual nanoplatelets

Preliminary characterization of OGNP-BPA samples, prepared at different carbonization temperatures (TCA), was performed by using TEM, HR-TEM, and SEM. Fig. 1 shows TEM-HR-TEM micrographs for samples prepared at the highest and lowest TCA, 973 K, Fig. 1a-c and, 673 K, Fig. 1b-d, respectively. In Fig. 1a and b, OGNP nanoplatelets of few micrometers in size are imaged by TEM where white arrows point to nanoplatelet borders. High transparency to electron passage, together with SEM measurements in Fig. 1f confirms the formation of very thin nanoplatelets, with thickness below 92.65 nm. Fig. 1c and d show a zoom-in of the nanoplatelet surface and provide evidence of randomly oriented graphitic clusters for both TCA = 973 and 673 K. Most likely, the observed randomness arises from the presence of oxygen functional groups attached to the surface and intercalated between the single layers. Intercalation is indeed expected to enhance the interlayer spacing, giving rise to a non-preferred stacking orientation along the c-axis. The multiple orientation of the graphitic grains has been further confirmed via electron diffraction (ED) measurements. Selected-area ED patterns (displayed as insets in Fig. 1c and d) show in both cases diffuse rings characteristic of polycrystalline structures.

Nevertheless, it is worth mentioning that diffracted rings are better defined for the sample prepared at TCA = 973 K, suggesting a higher local order. Although HR-TEM micrographs may look similar for different TCA, electron energy loss spectroscopy (EELS) measurements performed on the same systems [25,30] have demonstrated different sp^2 fraction (sp^2 character/(sp^2 + sp^3 characters)) of 66% and 87% for samples prepared at 673 and 973 K, respectively. In summary, TEM/HR-TEM and ED techniques suggest the formation of nanoplatelets consisting of randomly distributed graphitic grains with a short-range crystalline order, which can be improved by increasing TCA.

To conclude our analysis, Fig. 1e shows a comparison between X-ray diffraction (XRD) patterns acquired on reference graphite (in black) and a GO-BPA sample synthesized at 973 K (in orange). Red arrows indicate XRD peak position of simulated hexagonal graphite.

The peak shift observed at diffraction angles 25.50°, 43.02°, 52.60°, and 57.87° in the *002*, *100*, *004*, and *103* directions, respectively, were computed by first-principles calculation using the structure factor in a hexagonal simple configuration, given by $f_{hkl} = f[1 + \exp(\pi i[h(4/3) + k(2/3) + l(1)])]$ [37]; here, both terms were obtained by considering two atoms per unit cell [(0 0 0), (2/3 1/3 1/2)], and these peak shifts were
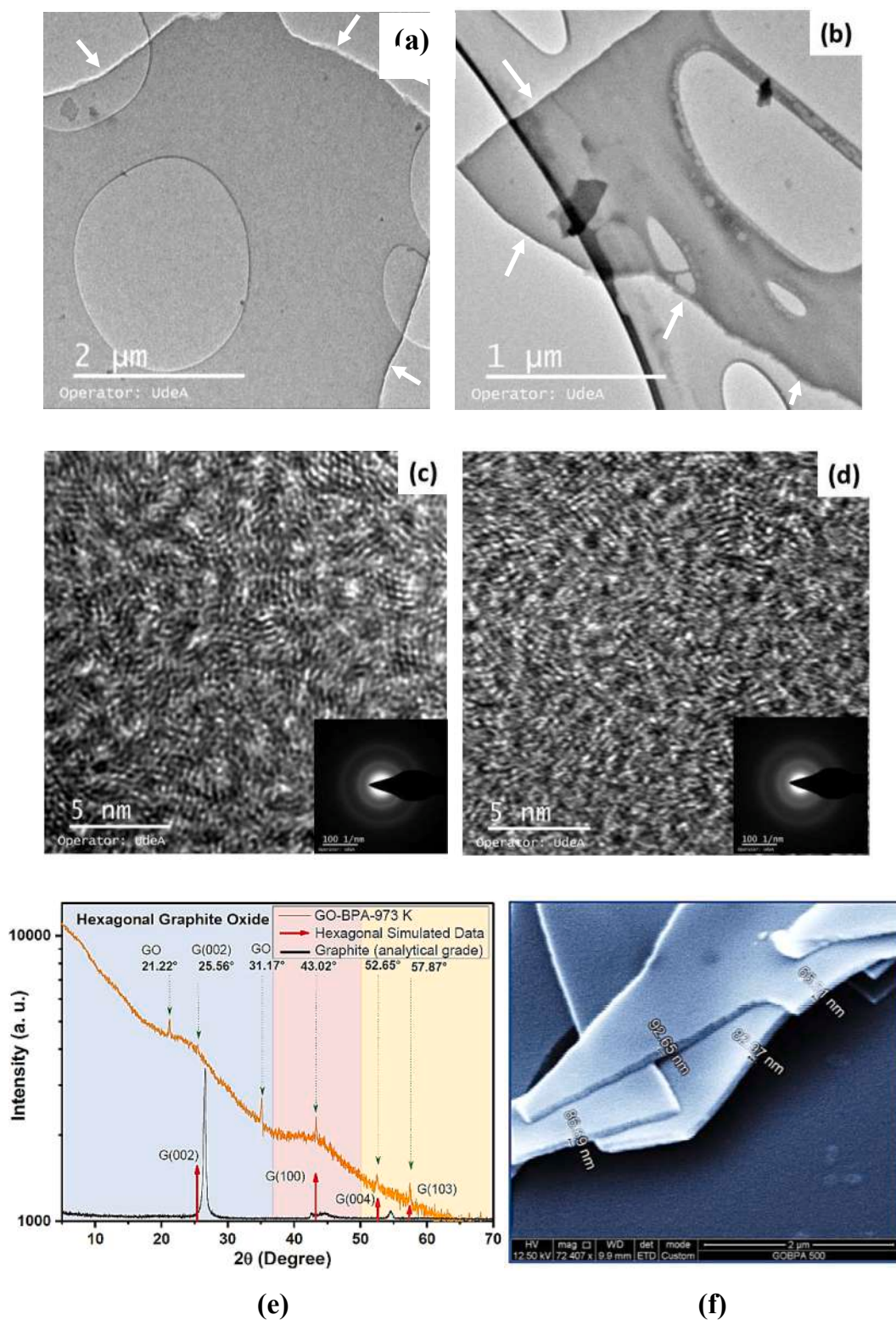
Fig. 1. TEM/HR-TEM micrographs of OGNP-BPA prepared at TCA = 973 K (a), (c); and with TCA = 673 K (b), (d). White arrows in (a) and (b) point to nanoplatelet borders. Insets show the electron diffraction patterns obtained for each TCA; (e) XRD pattern of the GO-BPA sample obtained at TCA = 973 K (in orange) and a graphite sample (in black). Red arrows indicate simulated peak position of a hexagonal graphite sample. (f) SEM image of four OGNP with edge thicknesses ranging from 65.51 to 92.65 nm. (For interpretation of the references to color in this figure legend, the reader is referred to the web version of this article.)

attributed to possible variations of the average length of carbon–carbon atoms being 2.461 Å rather than 2.456 Å. As reported by Li Hui *et al.*, [38] this behavior can be attributed to the presence of high density of defects and high stacking disorder. Finally, Fig. 1f shows a SEM image

indicating values of the OGNP thicknesses varying from 65.51 to 92.65 nm. Fig. 2a shows a SEM image of OGNP with hundreds of micrometers in lateral size, whereas Fig. 2b shows SEM micrographs of OGNP-BPA prepared at different TCA. Clear changes on surface morphology are
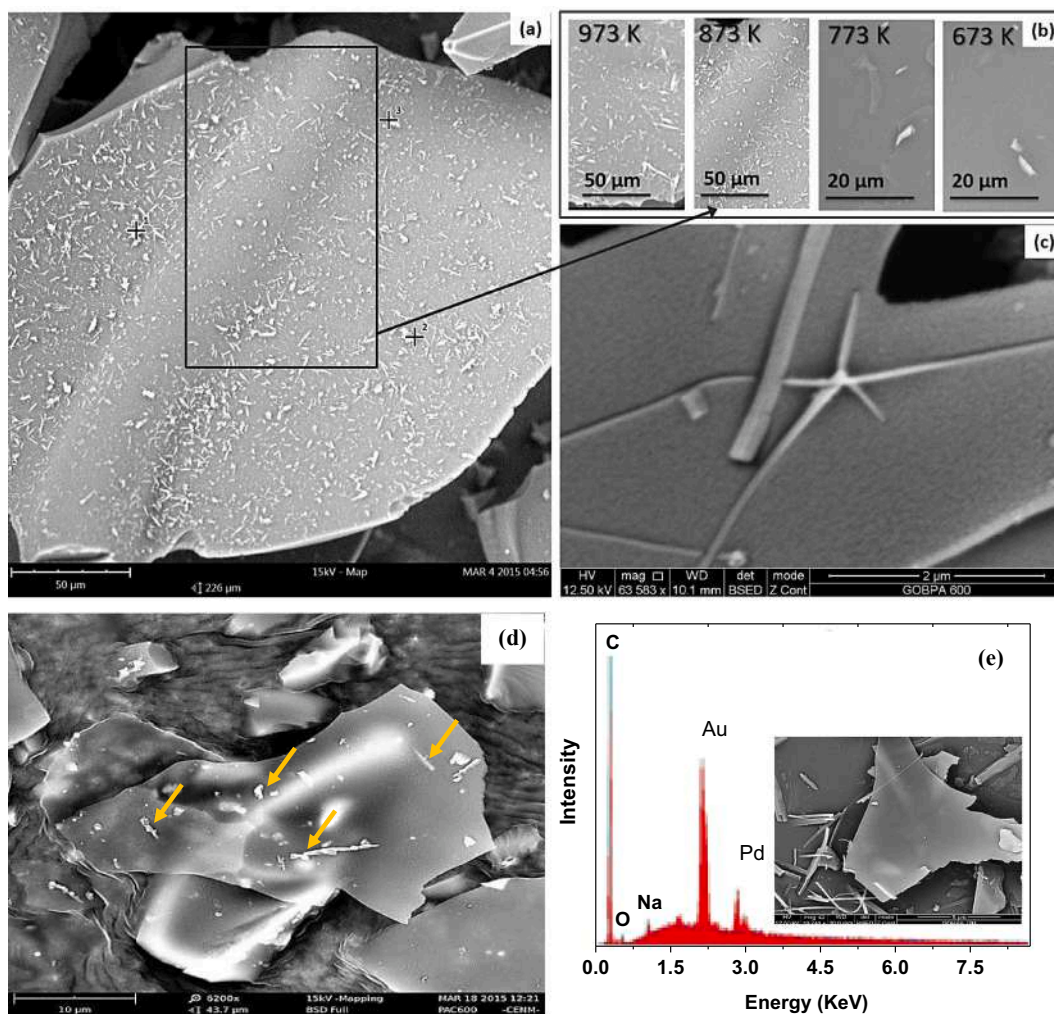
Fig. 2. (a) SEM image of OGNP prepared at 873 K. (b) SEM images taken for different TCA, from 673 to 973 K. (c) Zoom-in of SEM image of OGNP prepared at 773 K. (d) SEM image of OGNP prepared at 973 K. (e) EDS-SEM (inset) revealed Na presence in the OGNP prepared at 973 K with compositional analysis of C = 91.07%, O = 6.16%, and Na = 2.77%. The other peaks at 2.13 and 2.83 KeV correspond to the gold–palladium coating employed to improve the image of samples.

visible by increasing the carbonization temperature, indeed flat and smooth surfaces are observed at 673 and 773 K; cluster-like structures with brighter contrast become visible at higher TCA. The zoom-in for Fig. 2c reveals that such clusters do not lie on the surface, but are rather embedded within the platelets, modifying their topography and generating abrupt curvatures in the graphitic basal plane. Finally, Fig. 2d shows a SEM image of an OGNP decorated with clusters (orange arrows) of different lateral sizes and shapes. The chemistry of these clusters was obtained by performing local EDS analysis, resulting in Na composition, as presented in Fig. 2e for the 973 K sample; the inset shows the samples's SEM image. The mechanism for the formation of such Na-clusters is still not completely understood; however, it is worth mentioning that Na is expected to be absorbed as nutrient by the bamboo plants and, therefore, its presence in the pyroligneous acid used during fabrication can be expected.

3.2. Effect of defect density on room-temperature ferromagnetism

The reduction of GO, commonly carried out via chemical/thermal treatments allows for controlling defect density in the system [38]. The TCA has been previously demonstrated to be a valid tool for tuning the vibrational, structural, and electrical response of OGNP-BPA [30,31]; here, we demonstrate the direct effect of TCA on defect density, and indirectly, on room-temperature ferromagnetism.

The presence of defects in OGNP-BPA systems has been studied through RAMAN spectroscopy. In Fig. 3a, the Raman spectrum obtained on the sample prepared at TCA = 973 K shows G-band and D-band peaks at 1550 and 1330 cm^{-1}, respectively. Moreover, 2D and D + G bands are found around 2800 cm^{-1}, and their broadening suggests the presence of monolayers with edges, defects, and sp^2 regions, typical features of GO (more details in the reference) [31]. To correlate the intensity of the D-peak with the number of defects in the system, we studied the deconvolution of the Raman peaks, around the D-band, for TCA = 673, 773, 873, and 973 K.

As shown in the inset of Fig. 3a, the spectra could be deconvoluted into three characteristic peaks: G-band, D-band, and D'-band, with the latter associated with the presence of boundary defects. Observe that by increasing TCA, the ratio of the intensity of the defect bands (ID and ID') to that of the G-band (ID/IG and ID'/IG) increases monotonically, thus, indicating increased defect density (Fig. 3b), possibly attributed to desorption of organic compounds and multifunctional oxides due to the thermal decomposition involved in the synthesis method used. The defect density (n_D), as function of TCA, is plotted in Fig. 3c; here, n_D has been calculated by using equation (1) [40,41]:

$$n_D(cm^{-2}) = \sqrt[2]{7.3 \times 10^{-9}(1239.84/\lambda_L)^4 \left(\frac{I_D}{I_G}\right)} \tag{1}$$

In this expression, λ_L is the laser wavelength line at 632.81 nm, as
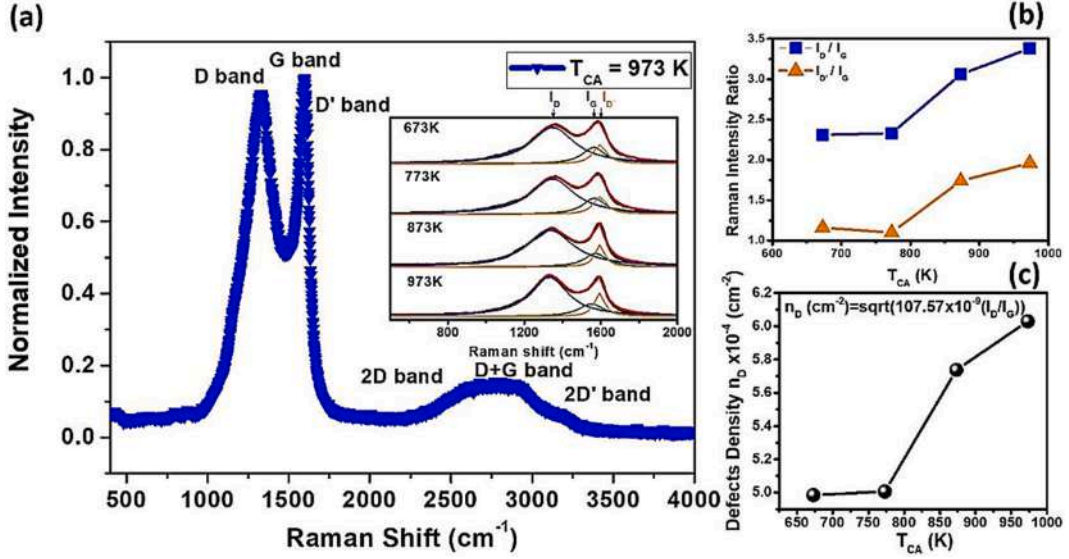
4

Fig. 3. (a) Normalized Raman spectra of OGNP-BPA synthetized at TCA = 973 K; inset: Lorentzian deconvolution fit around D, G, and D́ bands for TCA = 673, 773, 873, and 973 K; (b) evolution with TCA of the intensity ratio of D and D' to G band, ID/IG and ID'/IG; (c) dependence of defect density on TCA.

reported [40,41]. We observe an increase of the defect density from 5.0 $\times 10^{-4}$ to 6.0×10^{-4} cm^{-2} when increasing TCA, in good agreement with recently reported values in the range of 4.9×10^{-4} and 5.3×10^{-4} cm^{-2} [41]. Indeed, these results correlate well with the observation of increased density of Na-clusters, as observed by SEM. Fig. 4a shows magnetization measurements for the 673, 773, 873, and 973 K samples measured at 300 K in a field range from -6000 to $+6000$ Oe.

The ferromagnetic-like hysteresis loops are characterized by low magnetization saturation ranging from 2 to 40 memu/g that agree with values of 4–20 memu/g, associated with room temperature ferromagnetism in graphene-based materials, as reported by Yan Wan *et al.*, [42]. Sample holder magnetization has been introduced as reference. As shown in Fig. 4b, the OGNP samples exhibit low magnetic remanences ranging from about 1.5 memu/g for the 973, 873, and 773 K samples to 0.2 memu/g for the 673 K sample and low coercive fields ranging from 10 to 100 Oe, which agree with the value of 40 Oe as coercive field measured at room-temperature in rGO, as reported [42–44]. In addition, the magnetic remanence of 1.5 memu/g measured at 300 K in this work also agrees with the value of 1 memu measured at 300 K in rGO, as reported [45]. The inset of Fig. 4a shows the influence of the defect density on the saturation magnetization; it can be observed that saturation magnetization increases with defect density (and with TCA), possibly attributed to electron localization at defects that produce magnetic dipoles. Magnetic remanences around 1.5 memu/g are considerable values compared to soft ferromagnets, confirming the growing interest for low-cost graphite and OG technologies. Additionally, decreased saturation magnetization experimentally exhibited by the sample synthesized at TCA of 873 K, as seen in the inset of Fig. 4a, could be associated with the effects of ferromagnetic ordering by stacking of the different graphene oxide layers into the OGNP-BPA samples; this aspect requires more complementary characterization and it will be considered in the future publication by our group.

Ferromagnetic behavior was supported by using the temperature influence on saturation magnetization, as presented in Fig. 4c. Indeed, it can be observed that for decreasing temperatures, the saturation magnetization of the 973 K sample increases, as expected in soft ferromagnets. Moreover, the extrapoled Curie temperature suggests a theoretical value of 477 K in OGNP-BPA synthesized at 973 K, agreeing with the value of 500 K of Curie temperature in graphite samples, as reported by Ezquinazi *et al.,* and J. Cervenka [46,48]. The magnetism behavior exhibited experimentally by OGNP-BPA samples was described theoretically by employing the standard Brillouin function, given by

[48–50]:

$$M(H) = NgJ\mu_B \left[\frac{2J+1}{2J} coth\left(\frac{2J+1}{2J}x\right) - \frac{1}{2J} coth\left(\frac{x}{2J}\right) \right] \quad (2)$$

Here, $x = gJ\mu_B H/K_B T$, where N is the number of atoms per unit volume, which presents units of g^{-1}; g is the Landé factor equal to 2, as reported by M. Sepioni *et al.*, [48] in graphite material; J is the total angular moment; and μ_B is the Bohr magneton equal to $9.27400915(23) \times 10^{-24}$ JT^{-1} [48]. Expression (2) has two special cases, $J = 1/2$ and $J = \infty$, given by [49,50]:

$$M(H)_{(j=1/2)} = NgJ\mu_B [tanh(x)] \quad (3)$$

and

$$M(H)_{(j=\infty)} = NgJ\mu_B \left[coth(x) - \frac{1}{x} \right], \quad (4)$$

so called, Langevin function [49,50]. Expressions (3) and (4) are used to explain paramagnetic and ferromagnetic behaviors, respectively [49,50].

Fig. 4d and e presents the room-temperature experimental hysteresis loops of OGNP-BPA samples synthetized at TCA = 773 and 973 K, respectively; both were theoretically described through fit with the Brillouin function (BF) of expression (2), the paramagnetism (PM) function as equation (3) and ferromagnetism (FM) Langevin function is given by expression (4). The respective results of regressions were R^2 equal to 0.97347, 0.97297 and 0.99612 for the OGNP-BPA-773 K sample, and R^2 equal to 0.99396, 0.98935 and 0.99914 for the OGNP-BPA-973 K sample, by employing BF, PM, and FM functions, respectively. These results suggest that the FM Langevin function had the best theoretical fit of the experimental loop hysteresis in OGNP-BPA samples and, thus, these samples exhibited mainly ferromagnetism order at room temperature.

The best J values obtained via theoretical fitting by employing the FM Langevin function in expression (4), which were equal to 5967 and 21,084 in the OGNP-BPA-773 K and OGNP-BPA-773 K-973 K samples, respectively, as presented in Fig. 4d and e. These high values of J revealed that FM behavior is the main magnetism characteristic of OGNP-BPA samples. The estimations of magnetic moments were carried out by employing the relation of $\mu = gJ\mu_B$, for each 10,000 carbon atoms; then, the variations of these values were obtained from $\mu = 1.2\mu_B/A$ to $\mu = 4.2\mu_B/A$ in OGNP-BPA samples synthesized at TCA = 773
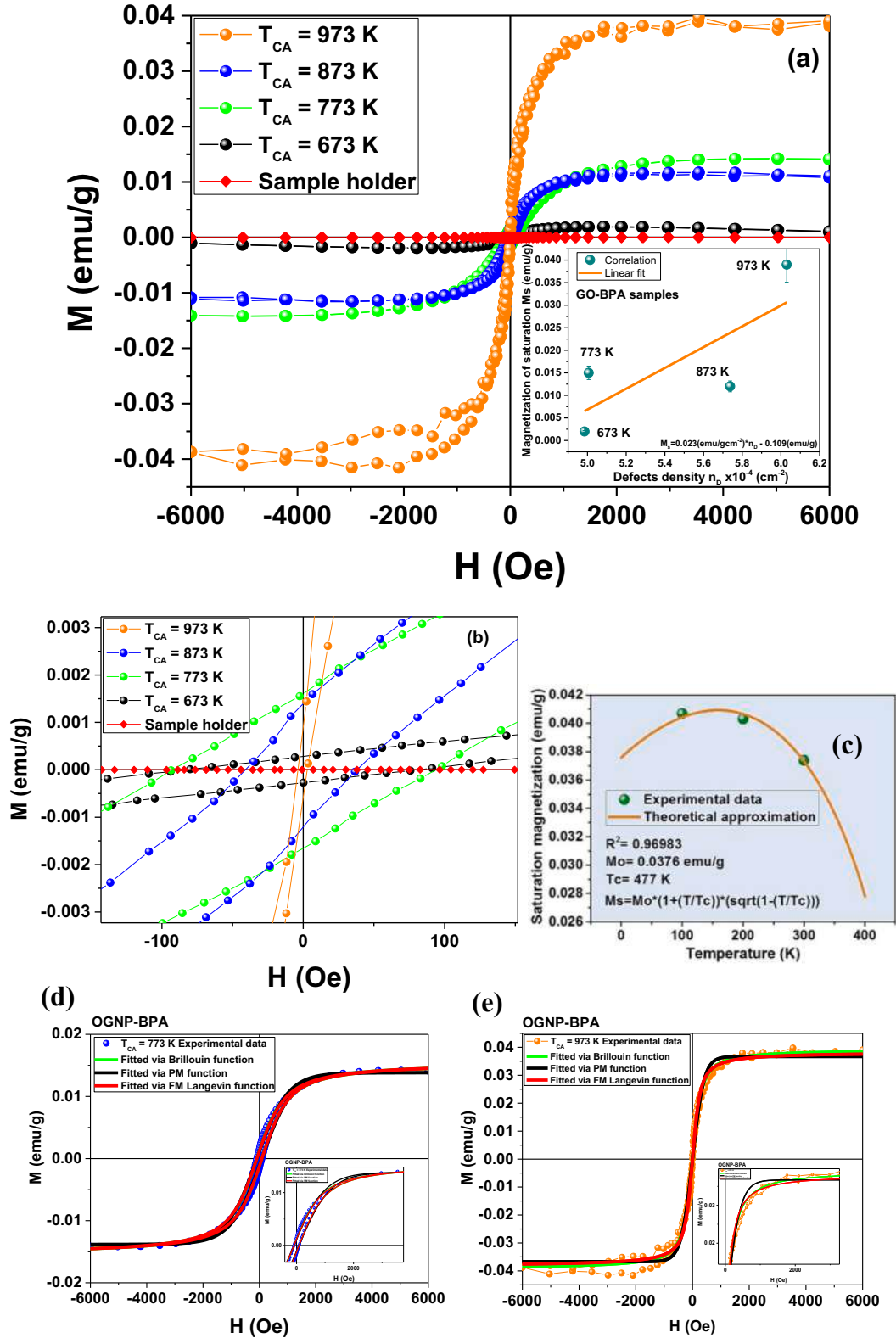
Fig. 4. (a) Magnetic hysteresis loops of OGNP-BPA powders synthetized at different carbonization temperatures, TCA = 673, 773, 873, and 973 K, measured at T = 300 K. The sample holder background (red diamonds) is also shown. No background subtraction has been performed. A correlation between saturation magnetization and defects density is presented in the inset. (b) Zoom-in around zero point showing magnetic remanence and coercive fields. (c) Temperature dependence of the saturation magnetization for the sample synthesized at TCA = 973 K. (d) and (e) Experimental magnetic hysteresis loops of OGNP-BPA at TCA = 773 and 973 K, respectively, both fitted by employing the Brillouin function of expression (2), paramagnetism (PM) function given by equation (3) and ferromagnetism (FM) Langevin function as expression (4). It was possible to observe that the best fitting was carried out by employing the FM Langevin function in the samples studied, which revealed possible FM order at room temperature in the OGNP-BPA samples. (For interpretation of the references to color in this figure legend, the reader is referred to the web version of this article.)

and 973 K, respectively. The high value of $\mu = 4.2\mu_B/A$ suggests FM order at room temperature, possibly induced by formations of boundary defect clusters as topographic defects, discussed through MFM measurements in Section 3.3. These variations of magnetic moments agree with the range of values varying from 1.732 to 2.707 μ_B/A, induced by grain boundary defects as theoretically calculated by Sudipta Dutta *et al.,* [14], as presented in Table 1.

Further, by considering estimations of the Raman cristalline sizes varying from 1.3 to 1.9 nm (estimations not shown here) and Raman boundary defect density varying from 5.0 to 6.0 $\times 10^{-4}$ cm^{-2} in OGNP-BPA synthesized at TCA = 673 and 973 K, respectively, as presented in Fig. 3c, the magnetic moment varies from 0.5 to 0.9 μ_B/defect; these were determined and agree with the range of value from 0.2 to 1.5 μ_B/defect, as reported by Oleg V. Yazyev *et al.,* [6], which describe theoretically ferromagnetic order induced mainly by boundary defects with vacancies. Therefore, these analyses of results suggest that OGNP-BPA samples exhibit ferromagnetism order at room temperature possibly induced by boundary defects cluster as topographic defects, agreeing with experimental observations through MFM measurements and discussed in Section 3.3.

Moreover, due to exotic magnetism behavior exhibited and observed experimentally on graphitic materials and reported by Kuzemsky [2], the question that usually arises is regarding the interpretations of the source of magnetic signal and several scenarios has been suggested, which predict the magnetism of graphitic materials: (i) presence of magnetic impurities or the magnetic proximity effect at the impurities [47]; (ii) volumetric magnetism of an ideal structure that contains alternating sp^2 and sp^3 domains hybridized with the carbon atoms [47,51]; (iii) magnetism at the atomic-scale caused by structural imperfections and defects [47,52–56].

Hence, to diluciate the source of the magnetic signal in OGNP-BPA samples, we discussed the following: (i) magnetic impurities can not explain fully the FM observed in OGNP-BPA samples, especially at room temperature, as discussed ahead. Table 2 presents the compositional measurements in OGNP-BPA samples by XPS (not shown here) and EDX techniques, and no magnetic impurities were detected. It is known that characterization techniques, like PIXE and RBS spectroscopies have been used to detect magnetic impurities in graphitic materials [57]; however, the respective analysis of results presented in Fig. 4a, suggests magnetic impurity abundance of 10% to 20%, which is closed in the range of XPS and EDX detections. In addition, in Table 2 it was possible to observe that increased TCA increased carbon content due to thermal decomposition that produces loss of oxygen content (5.25%−13.18%); also, magnetic impurities were not found. The N and Na impurity presence was observed in Table 2; these were less than 1% and 2% of carbon atoms and estimations of the contributions of these impurities in the magnetic moment varied from 0.45 to 9.00 $\times 10^{-3}$ μ_B, which correspond to three orders of magnitude less than values of magnetic moments varying from 1.2 to 4.2μ_B/A, as estimated by considering theoretical analysis of loop hysteresis, as presented in Fig. 4d and e. It is known that the case of the Fe cluster as impurity content of 1 µg per gram of graphite would contribute 2.2×10^{-4} emu/g approximately to magnetization and in case of the Fe$_3$O$_4$ cluster, this same contribution is 1.4×10^{-4} emu/g, approximately, assuming that these clusters behave as bulk materials [46]. These results reveal one and two orders of magnitude less than variations 2–40 memu/g of magnetization

saturation observed experimentally in OGNP-BPA samples in this work, as shown in Fig. 4a. Also, these results suggest Fe clusters varying from 10 to 20 µg/g, approximately, and these amounts of magnetic impurities cannot explain fully the FM order observed in OGNP-BPA samples, especially at room temperature, as presented in Fig. 4a. The XPS and EDX measurements are very sensitive to these amounts of Fe and Fe clusters and here these were not detected.

(ii) Considering volumetric magnetism by an ideal structure, which contains alternating sp^2 and sp^3 domains hybridized with carbon atoms, in this work, is unlikely because some theoretical studies suggest magnetizations from $\mu = 1.0\mu_B/A$ to $\mu = 1.2\mu_B/A$ for hydrogen chemisorption [7,8] and $\mu = 1.0\mu_B/A$ for OH-chemisorption [24], as shown in Table 1. These values are close to the $\mu = 1.2\mu_B/A$ value found in this work in a OGNP-BPA sample synthesized at TCA = 773 K, as already discussed in this section. However, merely hydrogen and hydroxyl chemisorption can not explain fully the FM observed in OGNP-BPA samples, especially at room temperature.

(iii) Magnetism at atomic-scale caused by structural imperfections and defects [47,52–56] is an important alternative to explain magnetism as possible source of magnetic signals in OGNP-BPA samples and discussed below. Some theoretical studies in defects responsible of ferromagnetism order in graphite suggest the likelihood that presence of strong topological disorder, like defects, will stabilize ferromagnetic order and frustrate antiferromagnetic order [58].

The correlation between magnetization saturation and defects density is presented in the inset in Fig. 4a. It is possible to observe that increased boundary defect density (by increasing TCA experimentally) increases magnetization saturation; this result suggests that ferromagnetic order can be induced by clusters of boundary defects as topographic defects observed by MFM measurements in OGNP-BPA samples, as discussed ahead. This result agrees with the estimations of magnetic moments of values varying from $\mu = 1.2\mu_B/A$ to $\mu = 4.2\mu_B/A$ in OGNP-BPA synthesized at TCA = 773 and 973 K, respectively, as discussed. These variations of magnetic moments is very close with the range of 1.732 to 2.707 μ_B/A, suggesting ferromagnetism order induced by grain boundary defects [14], as presented in Table 1.

In addition, estimations of magnetic moment through defect obtained within the range from 0.5 to 0.9 μ_B/defect; these values agree with values varying from 0.2 to 1.5 μ_B/defect reported by O. V. Yazyev *et al.,* [6] as discussed. These results revealed ferromagnetic order induced mainly by boundary defect cluster as topographic defects in OGNP-BPA samples, as presented and discussed ahead in Section 3.3.

Boundary defects inducing ferromagnetic order suggest magnetism at atomic-scale; however, in this work it was possible to observe experimentally though MFM technique the topographic defects possibly formed by boundary defect cluster around of Na agglomerations, as observed at 200 nm scale. The Na agglomerations are not responsible for ferromagnetic order in OGNP-BPA samples, specially at room temperature, given that Na has a strong ionization potential that produces intense electron–phonon interaction responsible for diamagnetism behavior, as known for zeolites [59]. The Na clusters were observed experimentally at micron scale, as presented in Fig. 2 and the boundary defects were estimated by Raman spectra analysis at nanometer scale, as reported by our group [37]; therefore, the contribution of boundary defects to magnetic properties is independent of Na cluster presence in OGNP-BPA samples. The focus here is related with the topographic

Table 2

Comparison between compositional measurements by XPS and EDX techniques in GO-BPA samples obtained at different TCA.

GO-BPA	XPS measurements				EDX measurements				Difference
TCA (K)	C-1s (%)	O-1s (%)	N-1s (%)	Na-1s (%)	C-K (%)	O-K (%)	N-K(%)	Na-K (%)	$\Delta O/O$ (%)
673	85.71	12.99	0.70	0.60	85.30	13.18	–	1.52	1.46
773	92.15	7.16	0.69	–	90.74	7.84	–	1.42	9.50
873	87.49	9.69	0.61	2.21	89.95	10.05	–	–	3.71
973	94.00	5.25	0.75	–	91.07	6.16	–	2.77	17.33

defects formed by clusters of boundary defects, where it is possible that the intercluster interaction and local electronic state coupling play an important role in the magnetic properties at 200 nm scale, as ferromagnetism behavior at room temperature exhibited by OGNP-BPA samples and discussed ahead.

3.3. Magnetism induced by topographic defects on individual nanoplatelets

The study of spontaneous magnetization in an OGNP film, prepared at TCA = 973 K, has been pursued through MFM experiments at room temperature and pressure. Fig. 5 compares topography and MFM maps acquired on a 5 μm × 5 μm scan area of sample surface. Black-to-white color scale has been used in Fig. 5a to map morphological features in a height range from 0 to 20 nm. Several brighter protrusions pop up from a mostly flat background (root mean square roughness is 2.3 nm), resembling "sodium clusters" as seen by SEM/EDS analyses.

The out-of-plane MFM signal was acquired simultaneously by implying a standard two-step technique and recording variation in cantilever oscillation phase due to the magnetic tip-sample interaction at a fixed lift height of 50 nm. Bright-blue-to-white color scale was used in Fig. 5b-c-d to map the magnetic signal, representative of attractive and repulsive interaction, respectively. By comparing Fig. 5a and b, one can notice that only two of the topographic clusters (enclosed in white dashed circles) contribute with a net non-zero out-of-plane magnetic signal. Fig. 5c-d show MFM maps acquired in the areas enclosing such clusters (black dashed squares in Fig. 5a), confirming that a non-zero out-of-plane spontaneous magnetization emerges from objects.

Among the clusters studied, some contributed to the MFM signal with fully out-of-plane magnetization, others appear to have an in-plane magnetization component. For instance, Fig. 6a and b show the magnetic contrast of the MFM maps reported in Fig. 5c and d, respectively, overlaid to the top-view of the corresponding 3D topographies. Fig. 6a is representative of the first situation (fully out-of-plane magnetization), whereas Fig. 6b exhibits tip-sample attraction (bright blue contrast) along the border of the cluster and tip-sample repulsion in a small region close to its right-hand edge (red contrast). Such behavior indicates the presence of an in-plane domain. In addition, in-plane magnetism and out-of-plane magnetism are related with the uneven morphology of the clusters, then the borders and the protrusions observed in topographic defects, as presented at 200 nm scale in Fig. 6b, could induce different magnetic properties in the OGNP-BPA samples, possibly caused by graphene-oxide monolayers at sample surfaces, which coats the topographic defects (formed in the center by sodium clusters, as presented in Fig. 2).

Therefore, on the border and protrusions of topographic defects, the clusters of boundary defects can exhibit possible inter-cluster interaction and local electronic-state coupling, which induce different magnetic properties in OGNP-BPA samples, as observed experimentally by employing MFM technique here and presented in Fig. 6b.

We have further studied the behavior of topographic clusters in presence of an external out-of-plane magnetic field (≈250 mT). Fig. 7 compares topography and MFM maps acquired on the same 3.4 μm × 3.4 μm scan area of the sample surface, in external magnetic field of 0 T and 250 mT. Again, clusters as high as 50–80 nm, seen in topography (Fig. 7a), slightly contribute to the out-of-plane magnetic signal (MFM map of Fig. 7b), when in zero external magnetic field (H = 0 T). However, when in presence of 250 mT, clear evidence of field-oriented out-of-plane magnetization is measured in correspondence of the clusters (Fig. 7c). Again, repulsive interaction is recorded on the top of each
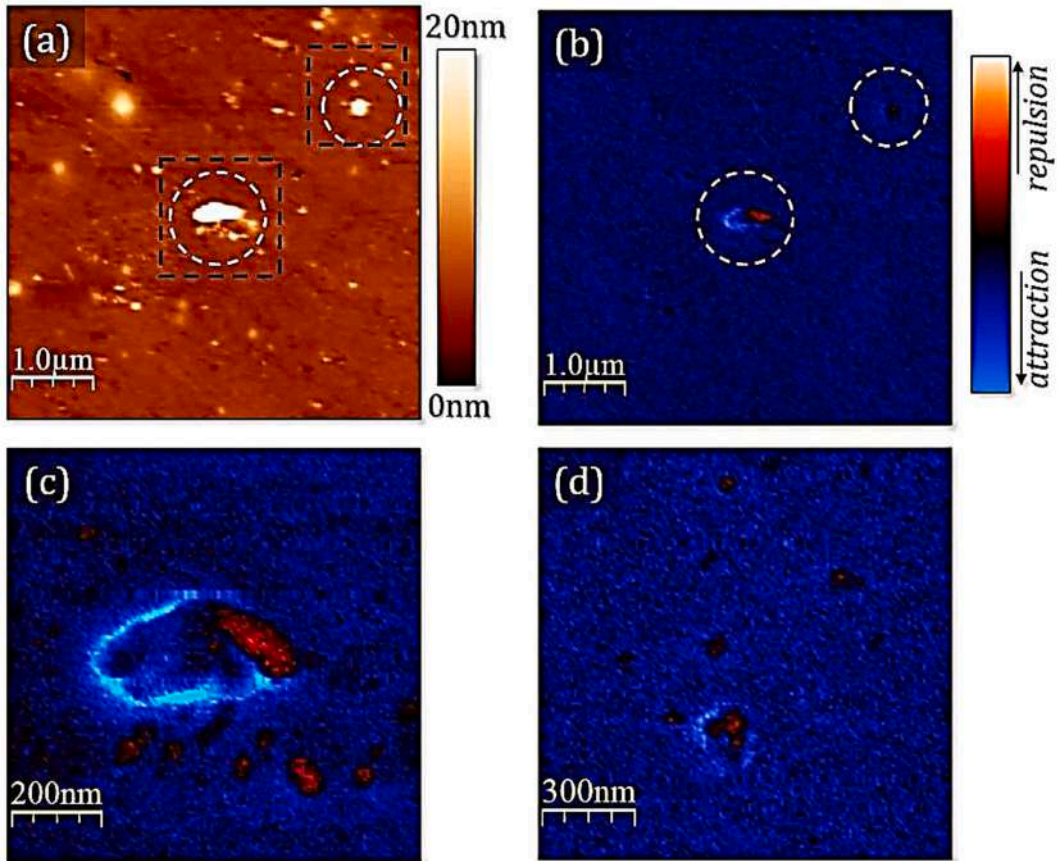

Fig. 5. (a) 5 μm × 5 μm topography of OGNP produced at 973 K; (b) corresponding MFM image at H = 0 T; (c)–(d) MFM images performed in the areas enclosed in black dashed squares in Fig. 5a.
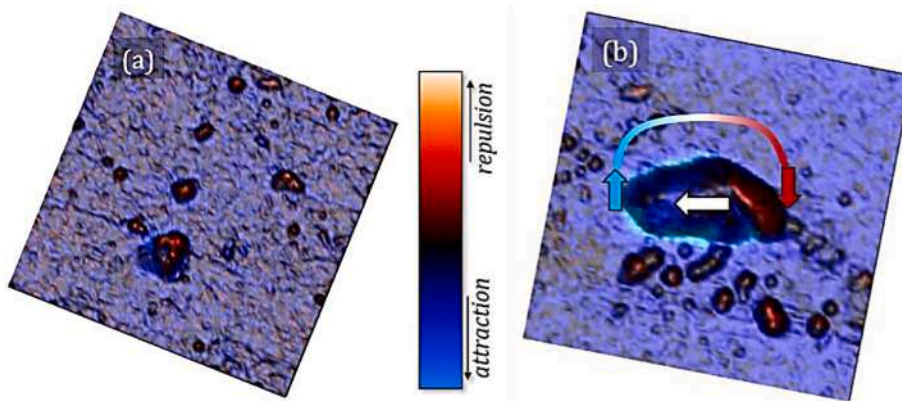
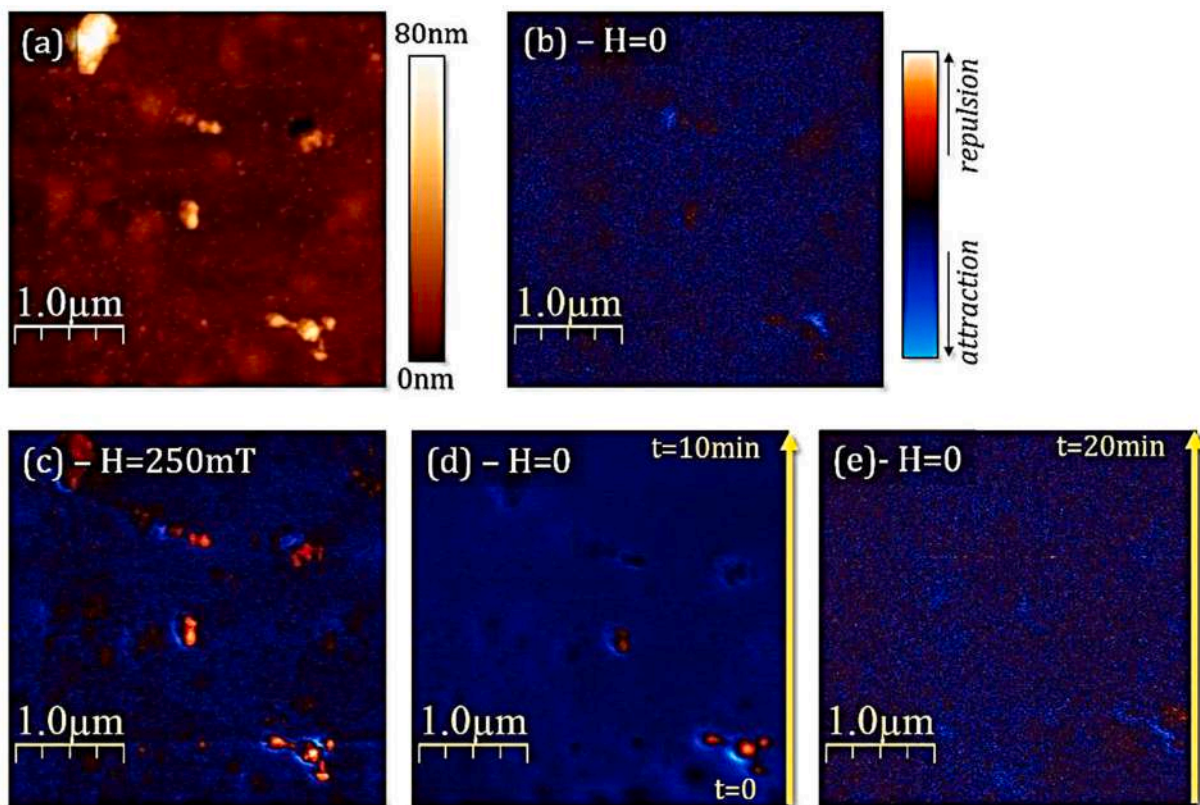**Fig. 6.** MFM signals overlaid on the corresponding 3D topographies for Fig. 5c and d.

Fig. 7. (a) 3.4 μm × 3.4 μm topography of OGNP produced at 973 K; corresponding MFM images at (b) H = 0 T, (c) H = 250 mT, (d)-(e) H = 0 T.

morphological object and attractive-interaction at their edge.

When removing the external field, starting yellow line in Fig. 7d, a non-zero out-of-plane magnetization is preserved for sometime, the bottom part of the MFM (Fig. 7d), acquired at the instant t = 0 min after removing the field, still shows a significant magnetic signal emerging from the clusters at the bottom-right corner of the image; while scanning the area from bottom to top, the magnetic signal of the clusters gradually decreases. After 10 min (Fig. 7d), the magnetic contrast is mostly restored to the initial conditions (Fig. 7b). After 20 min, very low magnetic signal is observed in Fig. 7e.

As shown in Fig. 8, the same experiment was repeated on a different area of the sample surface (5.1 μm × 5.1 μm in size). This time, no out-of-plane magnetic signal was recorded at H = 0 T, Fig. 8b, whereas a clear out-of-plane field-induced orientation of magnetization is measured at 250 mT, Fig. 8c. Again, when removing the external field (t

= 0 min – starting line of Fig. 8d-e), the out-of-plane magnetization decays gradually, restoring the initial conditions after 10-min scan.

Micro magnetic characterization carried out through MFM revealed that topographic defects are responsible for non-zero magnetization, which can lie both in the in-plane or out-of-plane directions. Which of the out-of-plane magnetism and in-plane magnetism is the main influence?

This aspect requires further quantitative and complementary characterization than that mentioned here and will be considered in a future publication by our group; however, by considering qualitative MFM analysis and assuming that topographic defects exhibit uneven morphology and the extensions of the border is greater than specific protrusions, as observed in Figs. 6–8; then, the border of topographic defects could include more clusters of boundary defects than the protrusions of topographic defects. Hence, in-plane magnetism could be the
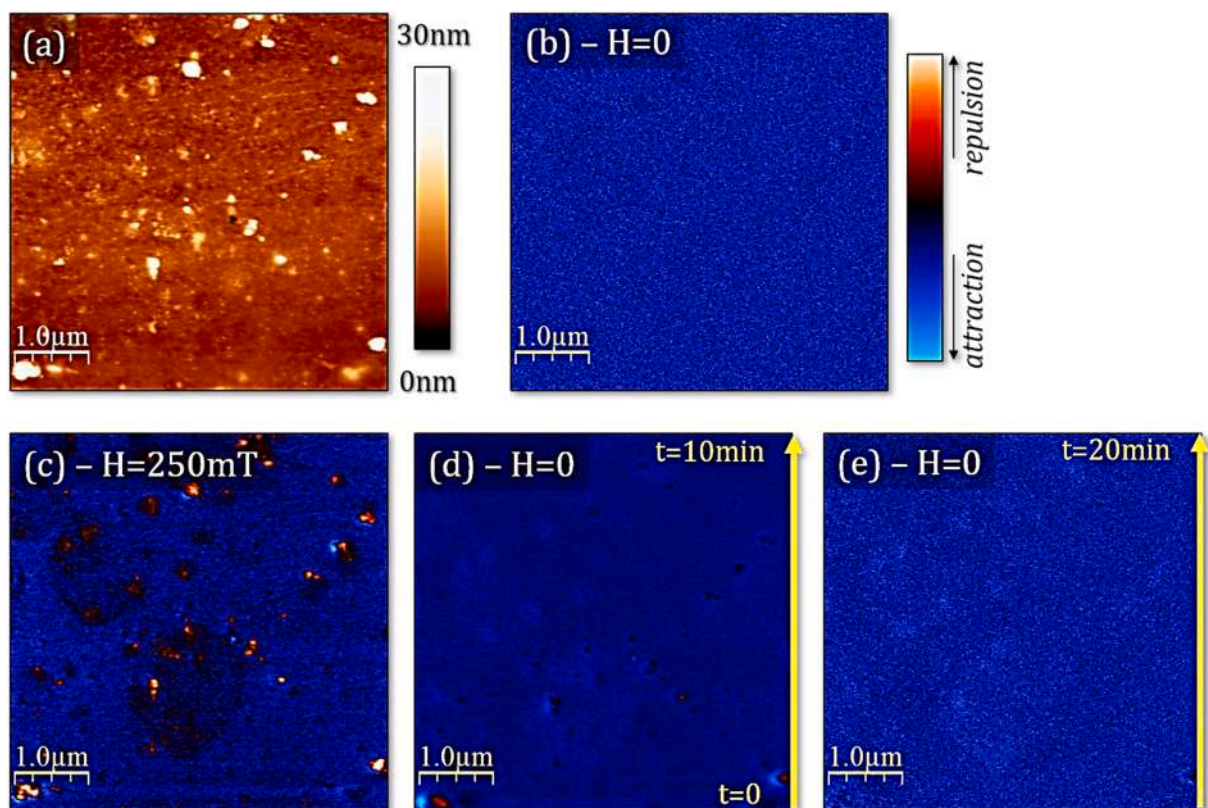
Fig. 8. (a) 5.1 μm × 5.1 μm topography of OGNP produced at 973 K; corresponding MFM images at (b) H = 0 T, (c) H = 250 mT, (d)-(e) H = 0 T.

main influence, the two magnetic moment contributions, do not cancel the output magnetic field, and both mechanisms enhance magnetism because of the geometric differences between borders and protrusions exhibited by topographic defects in the OGNP-BPA samples, as expected.

4. Conclusions

In summary, we have provided experimental evidence of room-temperature ferromagnetism induced by extended defects in oxidized-graphene nanoplatelets. Bulk magnetization measurements have shown that defect density correlates with TCA, giving rise to an enhanced FM signal. Furthermore, the micro magnetic characterization carried out through MFM revealed that the clusters are responsible for non-zero magnetization, which can lie both in the in-plane or out-of-plane directions. In OGNP-BPA, room-temperature ferromagnetism, combined with its semiconducting behaviour promise important implications for future applications of low-cost graphene and oxidized graphene-based technologies.

Author contributions

JP and HA initiated the project. JP, KG, and PP carried out the materials synthesis, microstructural characterization, Raman spectroscopy, and Magnetic measurements. JP, KG, PP, CG, FB, and AC wrote the manuscript with the inputs from JP and KG.

Declaration of Competing Interest

The authors declare that they have no known competing financial interests or personal relationships that could have appeared to influence the work reported in this paper.

References

[1] Klaus D. Sattler, Handbook of nanophysics principles and methods, CRC Press Taylor and Francis Group, FL, USA, 2011, 25.8.8., 25.15-16.

[2] L. Kuzemsky, Unconventional and exotic magnetism in carbon-based structures and related materials, Int. J. Modern Phys. B (IJMPB) 27 (11) (2013), 1330007-1-39.

[3] L. Kou, C. Tang, W. Guo, C. Chen, Tunable magnetism in strained graphene with topological line defect, ACS Nano 5 (2) (2011) 1012–1017.

[4] W. Tian, W. Li, Y.u. Wenbo, X. Liu, A review on lattice defects in graphene: types, generation, effects and regulation, Micromachines 8 (2017) 163.

[5] F. Banhart, J. Kotakoski, A.V. Krasheninnikov, Structural defects in graphene, ACS Nano 5 (1) (2011) 26–41.

[6] O.V. Yazyev, L. Helm, Defect-induced magnetism in graphene, Phys. Rev. B 75 (12) (2007), 125408-1-5.

[7] P.O. Lehtinen, A.S. Foster, Y. Ma, A.V. Krasheninnikov, R.M. Nieminen, Irradiation-induced magnetism in graphite: a density functional study, Phys. Rev. Lett. 93 (18) (2004), 187202-1-4.

[8] Ž. Šljivančanin, R. Balog, L. Hornekær, Magnetism in graphene induced by hydrogen adsorbates, Chem. Phys. Lett. 541 (2012) 70–74.

[9] Y. Ma, A.S. Foster, A.V. Krasheninnikov, R.M. Nieminen, Nitrogen in graphite and carbon nanotubes: magnetism and mobility, Phys. Rev. B 72 (20) (2005), 205416-1-6.

[10] D.W. Boukhvalov, S. Moehlecke, R.R. da Silva, Y. Kopelevich, Effect of oxygen adsorption on magnetic properties of graphite, Phys. Rev. B 83 (23) (2011), 233408-1-4.

[11] C.H. Hu, Y. Zheng, Y. Zhang, S.Q. Wu, Y.H. Wen, Z.Z. Zhu, Electronic and magnetic properties of silicon adsorption on graphene, Solid State Commun. 151 (17) (2011) 1128–1130.

[12] Y.-W. Son, M.L. Cohen, S.G. Louie, Half-metallic graphene nanoribbons, Nature 444 (7117) (2006) 347–349.

[13] F. Huttmann, D. Klar, N. Atodiresei, C. Schmitz-Antoniak, A. Smekhova, A.J. Martínez-Galera, et al., Magnetism in a graphene-4 f -3d hybrid system, Phys. Rev. B 95 (2017), 075427-1 8.

[14] S. Dutta, K. Wakabayashi, Magnetization due to localized states on graphene grain boundary, Sci. Rep. 5 (1) (2015), 11744-1-9.

[15] A. Sharma, V.N. Kotov, A.H. Castro, Neto, Effect of uniaxial strain on ferromagnetic instability and formation of localized magnetic states on adatoms in graphene, Phys. Rev. B 87 (2013), 155431-1-9.

[16] A.L. Kuzemsky, Statistical mechanics and the physics of many-particle model system, Phys. Part. Nucl. 40 (2009) 949–997.

[17] Tatiana L. Makarova, Bertil Sundqvist, Roland Höhne, Pablo Esquinazi, Yakov Kopelevich, Peter Scharff, Valerii A. Davydov, Ludmila S. Kashevarova, Aleksandra V. Rakhmanina, Magnetic carbon, Nature 413 (6857) (2001) 716–718.

[18] C.N.R. Rao, H.S.S. Ramakrishna Matte, K.S. Subrahmanyama, Urmimala Maitra, Unusual magnetic properties of graphene and related materials, Chem. Sci. 3 (1) (2012) 45–52.

[19] P. Esquinazi, D. Spemann, R. Höhne, A. Setzer, K.-H. Han, T. Butz, Induced magnetic ordering by proton irradiation in graphite, Phys. Rev. Lett. 91 (22) (2003), 227201-1-4.

[20] P. Esquinazi, R. Hohne, K.-H. Han, A. Setzer, D. Spemann, T. Butz, Magnetic carbon: explicit evidence of ferromagnetism induced by proton irradiation, Carbon 42 (2004) 1213–1218.

[21] M.A. Ramos, J. Barzola-Quiquia, P. Esquinazi, A. Muñoz-Martin, A. Climent-Font, M. García-Hernández, Magnetic properties of graphite irradiated with MeV ions, Phys. Rev. B 81 (21) (2010), 214404-1-16.

[22] T.L. Makarova, A.L. Shelankov, I.T. Serenkov, V.I. Sakharov, D.W. Boukhvalov, Anisotropic magnetism of graphite irradiated with medium-energy hydrogen and helium ions, Phys. Rev. B 83 (8) (2011), 085417-1-8.

[23] H. Ohldag, P. Esquinazi, E. Arenholz, D. Spemann, M. Rothermel, A. Setzer, et al., The role of hydrogen in room-temperature ferromagnetism at graphite surfaces, New J. Phys. 12 (2010) 123012-1–10.

[24] Tao Tang, Nujiang Tang, Yongping Zheng, Xiangang Wan, Yuan Liu, Fuchi Liu, Qinghua Xu, Youwei Du, Robust magnetic moments on the basal plane of the graphene sheet effectively induced by OH groups, Sci. Rep. 5 (1) (2015), 8448-1-6.

[25] J. Cervenka, M.I. Katsnelson, C.F.J. Flipse, Room-temperature ferromagnetism in graphite driven by two-dimensional networks of point defects, Nat. Phys. 5 (2009) 840–844.

[26] Apurva Sinha, Anzar Ali, Ajay D. Thakur, Ferromagnetism in graphene oxide, Mater. Today: Proc. (2020) 1–4.

[27] Amar Nath Yadav, Ashwani Kumar Singh, Pramod Kumar, Kedar Singh, Graphene-induced room temperature ferromagnetism in cobalt nanoparticles decorated graphene nanohybrid, Nanoscale Res. Lett. 15 (166) (2020) 1–8.

[28] Vineeta Shukla, Observation of critical magnetic behavior in 2D carbon based composites, Nanoscale Adv. 2 (3) (2020) 962–990.

[29] Juan Li, Rongli Cui, Yanan Chang, Huan Huang, Xihong Guo, Jiahao Wang, Ru Liu, Kui Chen, Jianglong Kong, Gengmei Xing, Baoyun Sun, Preparing dangling bonds by nanoholes on graphene oxide nanosheets and their enhanced magnetism, RSC Adv. 10 (60) (2020) 36378–36385.

[30] K. Gross, J.J. Prías-Barragán, S. Sangiao, J.M. De Teresa, L. Lajaunie, R. Arenal, et al., Electrical conductivity of oxidized-graphene nanoplatelets obtained from bamboo: effect of the oxygen content, Nanotechnology 27 (2016), 365708-1-10.

[31] J.J. Prías-Barragán, K. Gross, H. Ariza-Calderón, P. Prieto, Synthesis and vibrational response of graphite oxide platelets from bamboo for electronic applications: synthesis and vibrational response of graphite oxide platelets, Phys. Status Solidi A 213 (1) (2016) 85–90.

[32] J.J. Prías-Barragán, K. Gross, H. Ariza-Calderón, P. Prieto, in: Graphene oxide multilayers obtained from bamboo: new synthesis method, basic properties, and future electronic applications, Wiley Scrivener Publishing LLC, London UK, 2019, pp. 191–236.

[33] J.J. Prías-Barragán, K. Gross, H. Ariza-Calderón, P. Prieto, Graphene oxide multilayers: synthesis and possible applications in electronics, in: Latin American Electron Devices Conference (LAEDC), IEEE, 2019, pp. 61–64.

[34] J.J. Prías-Barragán, K. Gross, H. Ariza-Calderón, P. Prieto, Transport mechanisms study in graphene oxide multilayers obtained from bamboo as source material and possible applications in electronic, in: Revista de Divulgación Científica y Tecnológica, del Instituto Interdisciplinario de las Ciencias de la Universidad del Quindío, 2018, pp. 9–47.

[35] J.J. Prías-Barragán, N.A. Echeverry-Montoya, H. Ariza-Calderón, Fabrication and characterization of activated carbon and carbon nanoplatelets from guadua angustifolia Kunth for their application in electronics, Rev. Acad. Colomb. Cienc. Ex. Fis. Nat. 39 (2015) 444–449.

[36] J.J. Prías Barragán, K. Gross, José Darío Perea, Niall Killilea, Wolfgang Heiss, J. Christoph, H. Brabec, Ariza Calderón and Pedro Prieto, Graphene oxide thin films: synthesis and optical characterization, ChemistrySelect 5 (2020) 11737–11744.

[37] J.J. Prías-Barragán, Transport mechanisms study in graphite oxide platelets obtained from bamboo for possible applications in electronic, Doctoral Thesis, University of Valle, Colombia, 2018, pp. 1–209.

[38] Li Hui, Yang Chuan Zheng, Liu Fang, Novel method for determining stacking disorder degree in hexagonal graphite by X-ray diffraction, Sci. China Ser. B-Chem. 52 (2) (2009) 174–180.

[39] Virendra Singh, Daeha Joung, Lei Zhai, Soumen Das, Saiful I. Khondaker, Sudipta Seal, Graphene based materials: past, present and future, Prog. Mater Sci. 56 (8) (2011) 1178–1271.

[40] L.G. Cancado, A. Jorio, E.H. Martins Ferreira, F. Stavale, C.A. Achete, R.B. Capaz, Quantifying defects in graphene via Raman spectroscopy at different excitation energies, Nano Lett. 11 (8) (2011) 3190–3196.

[41] Anagh Bhaumik, Jagdish Narayan, Conversion of p to n-type reduced graphene oxide by laser annealing at room temperature and pressure, J. Appl. Phys. 121 (2017), 125303.

[42] Yan Wang, Yi Huang, You Song, Xiaoyan Zhang, Yanfeng Ma, Jiajie Liang, Yongsheng Chen, Room-temperature ferromagnetism of graphene, Nano Lett. 9 (1) (2009) 220–224.

[43] Guoqing Ning, Chenggen Xu, Ling Hao, Olga Kazakova, Zhuangjun Fan, Hao Wang, Kunxun Wang, Jinsen Gao, Weizhong Qian, Fei Wei, Ferromagnetism in nanomesh graphene, Carbon 51 (2013) 390–396.

[44] Siddharth Gupta, Jagdish Narayan, Non-equilibrium processing of ferromagnetic heavily reduced graphene oxide, Carbon 153 (2019) 663–673.

[45] Retno Asih, Erik Bhekti Yutomo, Deril Ristiani, Malik Anjelh Baqiya, Takayuki Kawamata, Masatsune Kato, et al., Comparative study on magnetism of reduced graphene oxide (rGO) prepared from coconut shells and the commercial product, Mater. Sci. Forum 966 (2019) 290–295.

[46] P. Esquinazi, A. Setzer, R. Höhne, C. Semmelhack, Y. Kopelevich, D. Spemann, et al., Ferromagnetism in oriented graphite samples, Phys. Rev. B 66 (2002) 1–10.

[47] J. Cervenka, The role of defects on electron behavior in graphene materials, Eindhoven: Technische Universiteit Eindhoven 1 (2009) 1–143.

[48] M. Sepioni, R.R. Nair, S. Rablen, J. Narayanan, F. Tuna, R. Winpenny, A.K. Geim, I. V. Grigorieva, Limits on intrinsic magnetism in graphene, Phys. Rev. Lett. 105 (20) (2010) 1–6.

[49] Stephen Blundell, Magnetism in condensed matter, in: Oxford Master Series in Condensed Matter Physics, 2001, pp. 1–238.

[50] A.S. Arrott, Approximations to Brillouin functions for analytic descriptions of ferromagnetism, J. Appl. Phys. 103 (7) (2008) 1–2.

[51] A.A. Ovchinnikov, V.N. Spector, Organic ferromagnets. New results, Synth. Met. 27 (3-4) (1988) 615–624.

[52] Noejung Park, Mina Yoon, Savas Berber, Jisoon Ihm, Eiji Osawa, David Tománek, Magnetism in all-carbon nanostructures with negative gaussian curvature, Phys. Rev. Lett. 91 (237204) (2003) 1–4.

[53] M. Fujita, K. Wakabayashi, K. Nakada, K. Kusakabe, Peculiar localized state at zigzag edge, J. Phys. Soc. Jpn. 65 (1996) 1920–1923.

[54] P.O. Lehtinen, A.S. Foster, Y. Ma, A.V. Krasheninnikov, R.M. Nieminen, Irradiation-induced magnetism in graphite: a density functional study, Phys. Rev. Lett. 93 (187202) (2004) 1–4.

[55] J.J. Palacios, J. Fernández-Rossier, L. Brey, Vacancy-induced magnetism in graphene and graphene ribbons, Phys. Rev. B 77 (195428) (2008) 1–14.

[56] V. Oleg, Yazyev, Magnetism in disordered graphene and irradiated graphite, Phys. Rev. Lett. 101 (037203) (2008) 1–4.

[57] D. Spemann, P. Esquinazi, A. Setzer, W. Böhlmann, Trace element content and magnetic properties of commercial HOPG samples studied by ion beam microscopy and SQUID magnetometry, AIP Adv. 4 (107142) (2014) 1–15.

[58] C. Daulan, A. Derré, S. Flandrois, J.C. Roux, H. Saadaoui, STM observations at the atomic scale of a tilt grain sub-boundary on highly oriented pyrolytic graphite, J. Phys. I France 5 (9) (1995) 1111–1117.

[59] Y. Nozue, T. Kodaira, S. Ohwashi, O. Terasaki, H. Takeo, Magnetic properties of alkali metal clusters in zeolite cages, Mater. Sci. Eng., A 217-218 (1996) 123–128.